processes

MDPI

Article

Numerical Simulation Study of the Optimization on Tubing-to-Sediment Surface Distance in Small-Spacing Dual-Well (SSDW) Salt Caverns

Lei Wang [1,2], Zheng Chu [1,2], Jiang He [1,2], Yujia Zhai [1,2], Junming Huang [1,2] and Haonan Yang [3,*]

[1] Sinopec Research Institute of Petroleum Engineering Co., Ltd., Beijing 102206, China
[2] Sinopec Key Laboratory of Geothermal Resources Exploitation and Utilization, Beijing 102206, China
[3] College of Petroleum Engineering, Northeast Petroleum University, Daqing 163318, China
* Correspondence: 238002020142@stu.nepu.edu.cn

Abstract: The small-spacing dual-well (SSDW) technique plays a crucial role in the establishment of underground salt cavern gas storage reservoirs. However, during the cavity dissolution and brine discharge processes, insoluble sediment is prone to being carried into the discharge tubing with the brine, leading to tubing blockages or clogging, which disrupts injection and withdrawal operations and severely affects both project efficiency and the safety of the gas storage facility. This study systematically analyzes the influence of the gap between the injection and discharge tubing and the surface of the sediment-on-sediment movement, deposition, and tubing safety in SSDW salt caverns. Through numerical simulations, this study investigates the influence of tubing layout on the internal flow field distribution of the cavern and the suspension behavior of sediment, revealing the changing trend of the risk of sediment entering the tubing at different distances. The results show that a rational tubing distance can significantly lower the risk of sediment backflow and tubing entry, while maintaining high brine discharge efficiency. Based on the simulation results, an optimized tubing layout design suitable for SSDW salt caverns is proposed, offering technical direction to guarantee the safe and effective functioning of underground salt cavern gas storage sites.

Keywords: small-spacing dual-well; dual-well cavern construction; salt cavern gas storage facility; insoluble sediment; flow field optimization

check for updates

Academic Editor: Qingbang Meng

Received: 6 January 2025
Revised: 16 January 2025
Accepted: 21 January 2025
Published: 24 January 2025

Citation: Wang, L.; Chu, Z.; He, J.; Zhai, Y.; Huang, J.; Yang, H. Numerical Simulation Study of the Optimization on Tubing-to-Sediment Surface Distance in Small-Spacing Dual-Well (SSDW) Salt Caverns. *Processes* **2025**, *13*, 322. https://doi.org/10.3390/pr13020322

Copyright: © 2025 by the authors. Licensee MDPI, Basel, Switzerland. This article is an open access article distributed under the terms and conditions of the Creative Commons Attribution (CC BY) license (https://creativecommons.org/licenses/by/4.0/).

1. Introduction

Entering the 21st century, natural gas has rapidly increased its share in the global energy use structure. This growth is attributed to continuous breakthroughs in both conventional and nonconventional oil and gas exploration and development technologies [1,2], as well as the swift growth of natural gas applications in heating, power generation, and automotive energy sectors. As a result, the global natural gas consumption industry has entered a phase of accelerated growth. In the last ten years, China's natural gas consumption has also entered a phase of swift expansion. However, due to the uneven distribution of natural gas reserves in China, the country has built multiple underground gas storage systems to effectively alleviate the natural gas supply pressure in the Central and Eastern parts of China. Despite this, with the continuous rise in industrial gas demand and further growth in urban gas consumption, the development of gas transportation infrastructure still faces significant challenges. As an essential component of natural gas infrastructure, underground gas storage

is essential for balancing gas supply and demand, as well as for managing seasonal peak usage, strategic reserves, and optimizing the layout of gas transmission networks.

Salt caverns, formed through controlled dissolution of salt deposits, are widely used as underground storage facilities for natural gas, hydrogen, and other energy resources due to their excellent geomechanical stability and sealing performance. These caverns are typically cylindrical or ellipsoidal in shape, with dimensions tailored to the geological conditions and storage requirements. The diameter of salt caverns generally ranges from 50 to 100 m, while their height can vary between 100 and 300 m, depending on the thickness of the salt layer and the purpose of the cavern [3]. The large-scale geometry of these caverns ensures substantial storage capacity while maintaining structural integrity under high-pressure conditions. In developing gas storage facilities in layered salt dome formations, due to geological limitations such as thin salt strata and thick intercalated layers, the existing single-well water-soluble cavern construction technology faces numerous challenges in cavern construction speed, interlayer treatment, and control of cavern shape. These challenges make it difficult to meet the growing natural gas storage requirements in China, as shown in Figure 1a. Therefore, there is a need to seek a more efficient cavern construction technology while developing additional formations with storage potential to address this issue. In 1997, Botho proposed a technique for salt cavern gas storage construction based on small-spacing dual-well water-soluble cavern technology [3]. This method connects the surface and underground salt layers using two vertical wells and employs horizontal well drilling technology to achieve bottom-hole connection. Compared to hydraulic fracturing for communication, this technique avoids issues such as poor directional communication in deep sections, cross-well slugging, water ingress in the formation, and low success rates in the later stages. The dual-well horizontal connection method not only effectively connects the bottom of the wells but also ensures the integrity and sealing of the cavern-surrounding rock. In small-spacing dual-well cavern construction technology, the two vertical wells are each equipped with a production casing and a cavern construction casing, and the dissolution process is conducted by injecting freshwater from one well and discharging brine from another well, utilizing a convection mechanism. During cavern construction, the injection and discharge sites can be modified based on the cavern's development, while the height of the cavern construction casing and oil cushion layer can be gradually raised to generate a cavern shape that meets gas storage needs. This process has significant advantages, including a simple brine extraction process, high dissolution rate, low accident rate, and easy management. Figure 1b clearly shows the process flow and equipment layout of the dual-well salt cavern construction method. Compared to traditional single-well cavern construction technology, small-spacing dual-well cavern construction technology demonstrates enormous potential and application prospects in improving dissolution efficiency, addressing complex geological conditions, and achieving higher gas storage construction efficiency.

Rock salt resources are abundant in China, with confirmed total reserves reaching 407.5 billion tons. The rock salt formations in China exhibit significant geological characteristics, such as shallow burial depth, numerous layers, and thin individual layers. Due to the layered nature of most of China's salt mines, the majority of them are difficult to dissolve, leading to a high proportion of insoluble substances in the salt rock [4,5]. Moreover, the geological conditions of China's salt rock deposits are relatively complex, which results in the production of large amounts of insoluble substances during the water-soluble cavern construction process, leading to deposition underneath the cavern. According to studies, the percentage of insoluble compounds in China's salt rock deposits can range from 5% to 20% [6], which is much higher than in salt rock deposits in other countries. For example, in Jintan, Jiangsu, on-site data indicate that insoluble substances account for 43% of the salt

cavern volume [7]. Research has shown that in China, the spatial proportion of insoluble sediments in the total volume of the cavern can reach more than 60% [8]. The presence of these insoluble substances poses multiple challenges to the development of salt rock deposits, not only increasing the technical difficulty of extraction but also significantly prolonging the construction period of water-soluble caverns in salt rock deposits. Additionally, the volume taken up by insoluble substances and the resultant tubing blockages also significantly raise the construction cost of salt cavern gas storage. Therefore, how to properly solve problems caused by insoluble sediment has emerged as a significant technical difficulty in China's salt cavern gas storage facilities. Currently, many scholars focus on the changes in the dissolution flow field and the shape control of the cavern in dual-well cavern construction [9,10], while research on insoluble sediment has not yet been fully developed. However, as the impact of insoluble residues on the cavern becomes more evident, scholars have started to study insoluble sediments, proposing predictive models for sediment accumulation shapes and methods for calculating porosity [4,7].

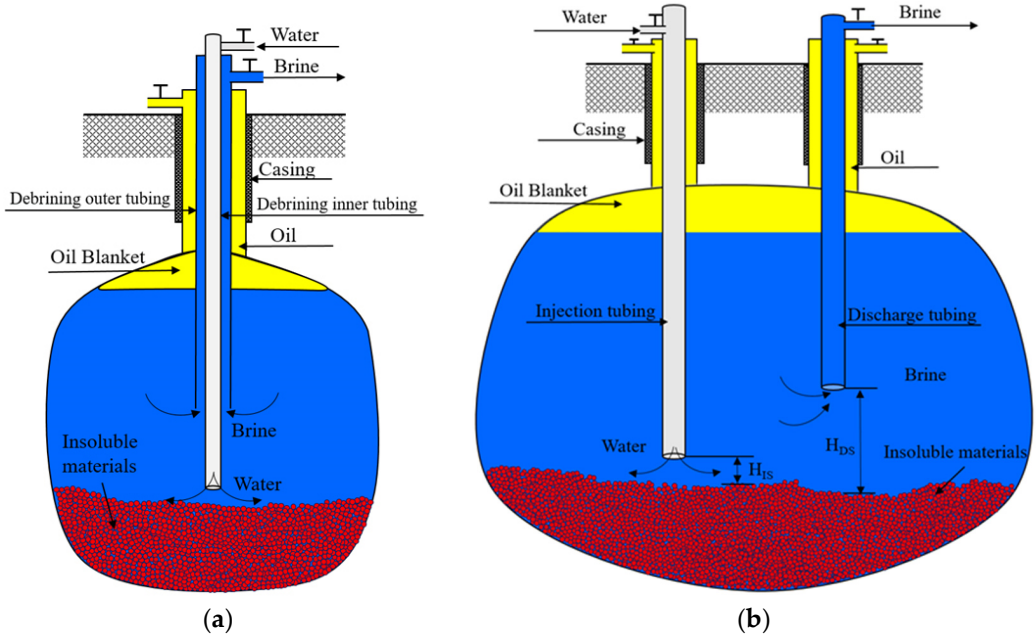

Figure 1. Gas storage schematic diagram: (**a**) schematic of the single-well cavern construction process; (**b**) schematic of the dual-well cavern construction process.

The gas injection and brine discharge process in a single well is a critical step in cavern construction. To maximize the utilization of cavern space, the central tubing should move downward as the liquid level drops, thereby displacing more brine from the cavern, as shown in Figure 2a. However, as the separation between the tubing outlet and the reduction of sediment surface develops, insoluble sediments are more likely to be carried along with the brine into the tubing, potentially causing blockages. Some researchers have therefore studied the secure distance between the central tubing and the sediment surface [11]. These sediments are typically composed of silt, clay minerals, and impurities from salt layer interbeds, with particles of varying sizes. Tiny insoluble particles may be drawn into the central tubing and transported along the tubing. As the distance from the surface decreases, the brine temperature gradually decreases, leading to brine supersaturation. These tiny insoluble particles act as nucleation sites for salt crystallization, causing blockages in the tubing. In addition, larger insoluble solid particles may also be drawn into the tubing, further contributing to blockages. In contrast to single-well construction, the flow field within a dual-well cavern is different, and the distribution of brine density within the cavern is uneven due to the dual-well process. Saturated brine tends to settle at the bottom

of the cavern [12,13]. To ensure faster and more efficient cavern dissolution, the discharge tubing in a dual-well system needs to extend to the cavern bottom to expel the saturated brine. During the dissolution process, sediments are disturbed and dispersed within the cavern due to the scouring action of the injection tubing. The downward extension of the injection tubing, which expels saturated brine, brings the tubing closer to the sediment surface, increasing the likelihood of insoluble sediments entering the tubing, as shown in Figure 2b. Therefore, the research on the safety distance between the tubing and sediment in the gas injection and brine discharge process of a single well does not apply to the cavern construction process of a dual-well system. This study aims to investigate the safe distance between the two tubing and the sediment surface in the dual-well cavern construction process, exploring the relationship between discharge rate, tubing size, and tubing extension distance, as well as sediment movement patterns. The goal is to identify solutions that prevent the ingress of insoluble substances into the discharge tubing, thereby avoiding blockages.

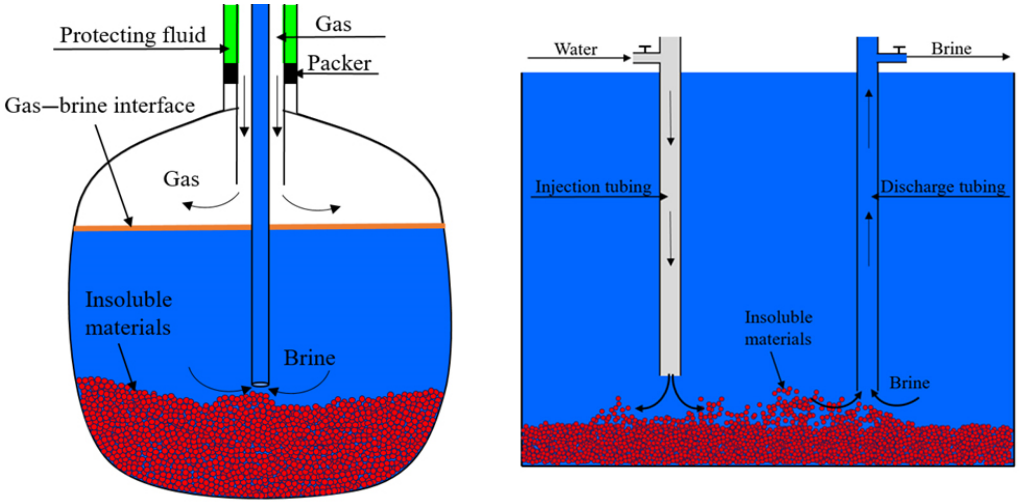

Figure 2. Schematic diagram of sediment impact at different stages: (**a**) single-well gas injection and brine discharge process; (**b**) insoluble sediment being suctioned into the discharge tubing during dual-well cavern construction.

2. Methodology

2.1. Mathematical Models

The focus of this study is on the optimization of the tubing-to-sediment surface distance in SSDW salt caverns during the brine extraction phase of construction. At this stage, the cavern is primarily filled with liquid phases (saturated brine and fresh water) and solid phases (sediments) with minimal or no gas phase involvement. Gas injection or storage typically occurs in the post-construction phase when the cavern has been fully developed. Hence, the continuity equations in this study only address the liquid and solid phases, as they are the dominant contributors to the dynamics of brine flow and sediment transport during the dissolution process. Solid-liquid two-phase flow, in which the solid and liquid phases are regarded as continuous media, is numerically simulated in this study using the Eulerian–Eulerian multiphase flow model. This approach describes the two-phase flow as continuous fields, avoiding direct tracking of the individual particle trajectories. Compared with the traditional Eulerian–Lagrangian method, this model offers higher computational efficiency and demonstrates significant advantages when dealing with multiphase flow problems involving high particle concentrations, making it more suitable for engineering applications due to its greater versatility and operational feasibility.

To improve the precision and dependability of the simulation results, the Realizable k-ε turbulence model was employed to describe turbulence's influence on the two-phase flow characteristics. In contrast to the standard k-ε model, the Realizable k-ε turbulence model can more accurately predict fluid behavior under complex conditions, such as strong vortices, flow separation, and non-isothermal flow fields. Its adaptability and stability have been widely recognized in complex flow field simulations. In particular, the Realizable k-ε model exhibits higher precision in predicting the rate of turbulence kinetic energy generation, anisotropic characteristics, and turbulence viscosity limitations.

Through the combination of the Eulerian–Eulerian multiphase flow model and the Realizable k-ε turbulence model, this study provides a comprehensive insight into the complex dynamic behavior of solid-liquid two-phase flow. The combination of model efficiency and high accuracy in turbulence treatment enables the in-depth exploration of the migration and deposition patterns of insoluble substances during the dual-well cavern construction process, providing reliable theoretical support and a numerical foundation for engineering design optimization.

Based on the particle dynamics theory [14], both the liquid and solid phases within the cavern are viewed as continuous, each satisfying the corresponding simultaneous equations of continuity. The liquid and solid phases' simultaneous equations of continuity can be written as follows [15,16]:

$$\frac{\partial(\alpha_l \rho_l)}{\partial t} + \nabla \cdot (\alpha_l \rho_l u_l) = 0 \tag{1}$$

$$\frac{\partial(\alpha_s \rho_s)}{\partial t} + \nabla \cdot (\alpha_s \rho_s u_s) = 0 \tag{2}$$

Momentum equation:

$$\frac{\partial(\alpha_l \rho_l u_l)}{\partial t} + \nabla \cdot (\alpha_l \rho_l u_l u_l) = -\alpha_l \nabla p + \nabla \cdot (\alpha_l \tau) + \alpha_l \rho_l g - \beta(v_l - v_s) \tag{3}$$

$$\frac{\partial(\alpha_s \rho_s u_s)}{\partial t} + \nabla \cdot (\alpha_s \rho_s u_s u_s) = -\alpha_s \nabla p - \nabla p_s + \nabla \cdot (\alpha_s \tau) + \alpha_s \rho_s g + \beta(v_1 - v_s) \tag{4}$$

Within the formulas, the subscripts l and s represent the fluid and insoluble sediment phases within the cavern, respectively; α denotes the volume fraction; ρ represents the density in g/cm^3; u is the velocity vector; p is the pressure in Pa; p_s is the solid phase pressure in Pa; τ is the stress tensor in N/m^2; g is the gravitational acceleration in m/s^2; β denotes the coefficient for momentum transfer between phases.

The formula for the solid phase pressure p_s is given by [17]:

$$p_s = \alpha_s \rho_s \Theta_s + 2\rho_s(1 + e_{ss}){\alpha_s}^2 g_{0,ss} \Theta_s \tag{5}$$

In the formula, represents the particle collision restitution coefficient; Θ_s represents the particle temperature, in m^2/s^2; and $g_{0,ss}$ stands for the radial distribution function.

The definition of $g_{0,ss}$ is:

$$g_{0,ss} = \left[1 - \left(\frac{\alpha_s}{\alpha_{s,\max}}\right)^{\frac{1}{3}}\right]^{-1} \tag{6}$$

The definition of Θ_s is:

$$\Theta_s = \frac{1}{3} u_{s,i} u_{s,i} \tag{7}$$

Collision, motion, and friction viscosities make up the solid phase viscosity in the dual-phase model [18,19]:

$$\mu_s = \mu_{s,col} + \mu_{s,kin} + \mu_{s,fr} \tag{8}$$

Formulations for collision viscosity $\mu_{s,col}$, motion viscosity $\mu_{s,kin}$, and friction viscosity $\mu_{s,fr}$ are presented below:

$$\mu_{s,col} = \frac{4}{5}\alpha_s\rho_s d_s g_{0,ss}(1+e_{ss})\left[\frac{\Theta_s}{\pi}\right]^{1/2}\alpha_s \tag{9}$$

$$\mu_{s,\,\mathrm{kin}} = \frac{10\rho_s d_s\sqrt{\Theta_s\pi}}{96\alpha_s(1+e_{ss})g_{0,ss}}\left[1+\frac{4}{5}g_{0,ss}\alpha_s(1+e_{ss})\right]^2\alpha_s \tag{10}$$

$$\mu_{s,fr} = \frac{p_s\sin\phi}{2\sqrt{I_{2D}}} \tag{11}$$

The resistance of particles to compression and expansion during flow is known as volume viscosity. Volume viscosity was defined by Lun et al. [20] as:

$$\lambda_S = \frac{4}{3}\alpha_S^2\rho_S d_s g_{0,ss}(1+e_{ss})\left[\frac{\Theta_S}{\pi}\right]^{1/2} \tag{12}$$

The Huilin–Gidaspow et al. [21] method is used to calculate the momentum exchange coefficient between the solid and liquid phases, which incorporates both the Ergun model and the Wen and Yu model. The formula is written as follows:

$$\beta_{Huilin\text{-}Gidaspow} = \varphi\beta_{Ergun} + (1-\varphi)\beta_{Wen\&Yu} \tag{13}$$

$$\varphi = \frac{\arctan[262.5(\alpha_s-0.2)]}{\pi} + 0.5 \tag{14}$$

When $\alpha_1 \leqslant 0.8$,

$$\beta_{Ergun} = 150\frac{\alpha_s(1-\alpha_1)\mu_1}{\alpha_1 d_s^2} + 1.75\frac{\rho_1\alpha_s\left|\vec{u_s}-\vec{u_1}\right|}{d_s} \tag{15}$$

When $\alpha_1 > 0.8$,

$$\beta_{Wen\&Yu} = \frac{3}{4}C_D\frac{\alpha_s\alpha_1\rho_1\left|\vec{u_s}-\vec{u_1}\right|}{d_s}\alpha_1^{-2.65} \tag{16}$$

C_D represents the drag coefficient [22]:

$$C_{\mathrm{D}} == \begin{cases} \frac{24}{Re_s}(1+0.15Re_s^{0.687}) & (Re_s \leqslant 1000) \\ 0.44 & (Re_s > 1000) \end{cases} \tag{17}$$

The particle Reynolds number Re_s can deem to be [23]:

$$Re_s = \frac{\rho_1 d_s\left|\vec{u_s}-\vec{u_1}\right|}{\mu_1} \tag{18}$$

Within the formulas, d_s represents the particle diameter in meters. The stress tensor expressions for insoluble sediments and brine are as follows:

$$\overline{\overline{\tau_l}} = \mu_l\left\{\left[\nabla\vec{u_l} + \left(\nabla\vec{u_l}\right)^T\right] - \frac{2}{3}\left(\nabla\cdot\vec{u_l}\right)\overline{\overline{I}}\right\} \tag{19}$$

$$\overline{\overline{\tau_s}} = \mu_s\left[\nabla\vec{u_s} + \left(\nabla\vec{u_s}\right)^T\right] + \left(\zeta_s - \frac{2}{3}\mu_s\right)\left(\nabla\cdot\vec{u_s}\right)\overline{\overline{I}} \tag{20}$$

Within the formulas, I represents the unit vector; μ_l and μ_s are the fluid viscosity and shear viscosity, respectively, in Pa·s; and ζ_s is the solid-phase volume viscosity, in Pa·s.

2.2. Model Structure and Boundary Conditions

To investigate the sediment movement patterns during the SSDW salt cavern construction process, simulations were conducted using actual cavern parameters. The cavern shape and size were referenced from production cases and related research applied in China [24], The geometric model of the fluid domain used for the simulation was approximated to be elliptical, as shown in Figure 3, where R_1, R_2, and R_3 are the curvature radii of the model boundary. In this study, the rock mass is assumed to be homogeneous without considering interlaminar heterogeneity or fractures, which is a simplification commonly used in numerical simulations focusing on fluid dynamics and sediment transport in salt caverns. The overall model height is 120 m, with a maximum cavern diameter of 70 m, a minimum diameter of 20 m, and a 10 m spacing between the injection tubing and discharge tubing.

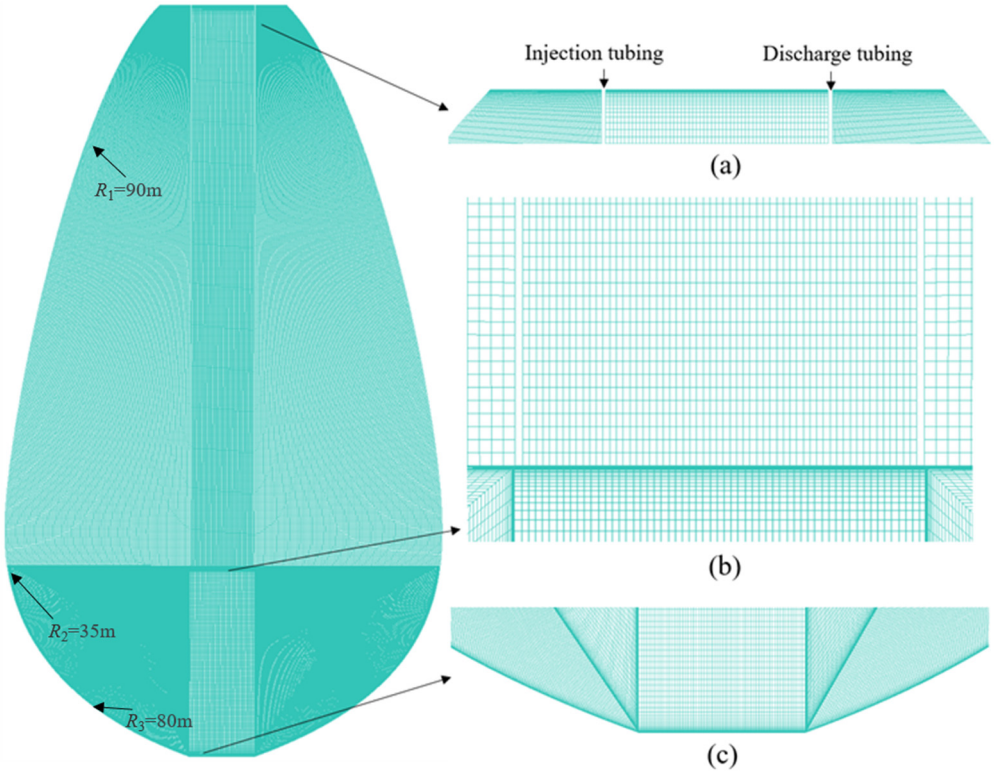

Figure 3. Schematic of the computational domain and mesh: (**a**) mesh at the top of the cavern; (**b**) mesh at the discharge tubing outlet; (**c**) mesh at the bottom of the cavern.

A block-structured grid method was used to divide the entire solution domain into several small blocks, each with structured grids [25,26]. The blocks are connected, and the grids around the cavern and the surrounding injection and discharge tubing were refined to enhance adaptability, providing convenience for the subsequent analysis of the flow field around the casing. The sum of grid cells is 183 and 418, and the grid quality check is shown in Figure 4. The grid quality can be intuitively represented by a bar chart, where the horizontal axis represents the grid quality, with a value range of 0 to 1, where 1 is the best, 0 is the worst, the closer to 1, the closer the grid shape is to the standard shape, and the higher the quality, while the vertical axis represents the number of grids for grid quality and the blue arrows indicate that the value is much larger than the upper limit corresponding to the vertical axis.. In the model in this study, the average grid quality level is 0.988.

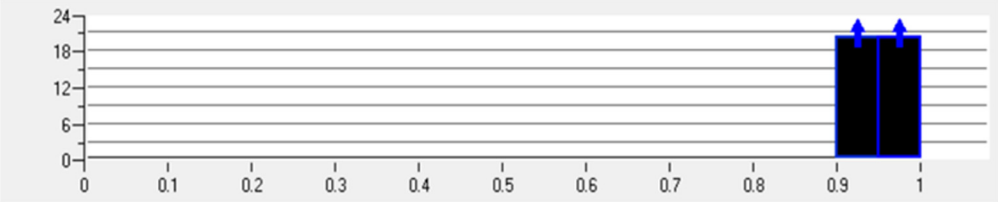

Figure 4. Model mesh quality.

The Eulerian–Eulerian multiphase flow model serves as the foundation for this study and adopts a transient calculation method to examine how the flow field affects the flow of insoluble material during SSDW cavern construction. The study focuses on the analysis of the following five factors, as shown in Table 1: injection flow rate, insoluble sediment diameter, the size of the tubing, and the separation between the injection and discharge tubing and the sediment surface. The distances from the injection tubing and discharge tubing to the sediment surface are denoted as H_{IS} and H_{DS}, respectively, as shown in Figure 1b. When exploring the effect of one factor on the sediment, the other parameters are kept constant for a single-factor analysis.

Table 1. Parameters and range of variation for numerical simulations.

Variables	Values
Injection Flow Rate, Q (m^3/h)	90, 120, 140, 160
Sediment Diameter, d (mm)	0.5, 1, 3, 5
Distance from Injection Tubing-to-Sediment Surface, $H_{IS}d$ (m)	0.3–2
Distance from Discharge Tubing-to-Sediment Surface, $H_{DS}d$ (m)	0.3–2
Tubing Diameter, D (mm)	114.3, 127, 139, 168.28
Tubing Diameter, D (mm)	2300, 2400, 2500, 2600

The sediment particles are assumed to be spherical. Taking the example of Jiangsu Jintan, the insoluble sediment's density spans from 2300 to 2600 kg/m^3. The minimum sediment diameter is 0.75 mm, and the maximum diameter is 20 mm, occupying approximately one-third of the cavern volume. The maximum flow velocity at the injection port is 6 m/s. Based on studies of sediment movement in single-well caverns, when the sediment diameter exceeds 5 mm, these particles are less likely to be impacted by the flow field since their initiation velocity is far higher than the maximum injection flow velocity inside the cavern. Furthermore, a comparatively tiny percentage of silt particles are larger than 5 mm. Consequently, the main focus of this research is the movement patterns of sediment particles with diameters ranging from 0 to 5 mm, with the particle diameter range chosen as 0 to 5 mm [11]. For the actual engineering parameters in Jiangsu Jintan, the remaining space inside the cavern is filled with saturated brine with a density of 1200 kg/m^3. The medium inside the tubing is fresh water, with a density of 1000 kg/m^3 and a viscosity of 1.003×10^{-3} kg/(m·s).

2.3. Model Verification

To ensure the validity and accuracy of the numerical simulation results, the SSDW numerical simulation results are compared with the single-well scenario. Figure 5 shows the critical velocity of particles sucked into the tubing simulated under the Euler two-fluid condition and the experimental results of Wang [11]. The results show that the numerical simulation results are highly consistent with the existing experimental data, with an average error of 9.82%. Under the Euler two-fluid condition, the model can accurately predict the movement behavior of insoluble sediments under the tubing.

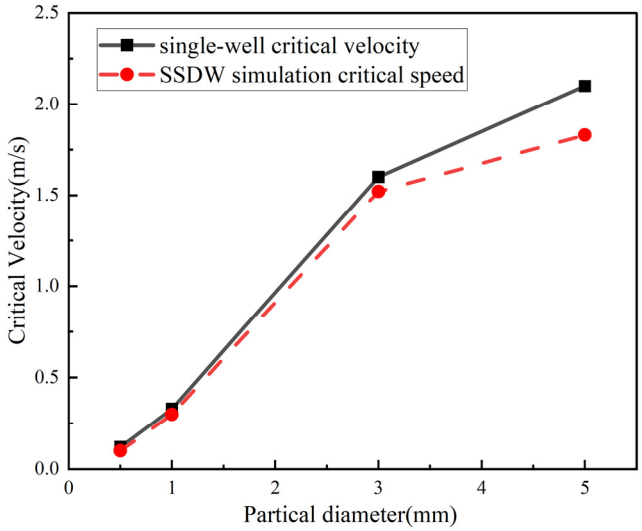

Figure 5. Validation for present prediction with experiment results from Wang.

3. Simulation Results Analysis and Discussion

3.1. Numerical Simulation Results

The SSDW cavern construction process involves two vertical wells and more complex flow field distribution characteristics, which make the forces acting on the insoluble sediment more complicated. During the cavern dissolution process, the flow field formed by the injection tubing directly affects the flow state inside the cavern and further plays a crucial role in the flow field around the discharge tubing. This flow field not only determines the dissolution efficiency of the brine but also significantly influences the movement trajectory, distribution, and risk of insoluble sediment entering the discharge tubing. The simulation results show that the area affected by the water flow entering the injection tubing only changes significantly above the insoluble sediments, and the impact on other areas is not obvious, as shown in Figure 6a. Therefore, this study only analyzed the area between the insoluble sediments and the injection and discharge tubing. When high-speed fluid is injected through the injection tubing, a strong jet flow field is formed near the injection port. This region exhibits a significant velocity gradient and disturbance intensity, with a particularly noticeable disturbance effect on the brine inside the cavern. At the center of the jet flow field, the velocity is the highest and gradually decays as the distance from the injection port increases, showing typical jet diffusion characteristics. As the injection flow rate increases, the velocity near the injection port rises, the jet diffusion range expands, and the disturbance intensity strengthens. This high-intensity disturbance not only has a stronger scouring ability on the sediment at the bottom of the cavern but also potentially causes sediment particles to enter a suspended state, migrating towards the discharge tubing along with the fluid motion, as shown in Figure 6b. Moreover, the jet flow field formed by the injection tubing superimposes with the natural flow within the cavern during the discharge process, making the flow field near the discharge tubing more complex. If the flow velocity near the discharge tubing is high, these particles may be entrained into the discharge tubing, leading to clogging issues. Figure 7 shows the distribution of velocity contour plots near the injection tubing and discharge tubing under different operating conditions during the dual-well cavern construction process. The calculation results indicate that the closer the distance between the injection tubing and discharge tubing, the denser the velocity contours, and the higher the flow velocity. As the distance between the injection tubing and discharge tubing increases, the contour lines gradually become sparse, and the flow velocity significantly decreases. The flow velocity directly beneath the injection tubing reaches its maximum, showing that

this area is most affected by the brine flow field disturbance. When the injection tubing is placed close to the insoluble sediment surface, particles are easily lifted or entrained by the flow from the injection tubing, causing the insoluble particles to float in the cavern's fluid. Under the influence of the flow field from the discharge tubing expelling saturated brine, the particles are most likely to be drawn into the discharge tubing. Additionally, the high-velocity water flow injected from the injection tubing creates a strong disturbance flow field, and its position and flow rate directly affect the flow velocity distribution in the bottom area of the cavern. When the injection velocity is high, the brine velocity near the discharge tubing significantly increases. Therefore, under the small-spacing dual-well cavern construction process, the high kinetic energy flow produced by the injection tubing further increases the risk of insoluble particles being drawn into the discharge tubing near its opening.

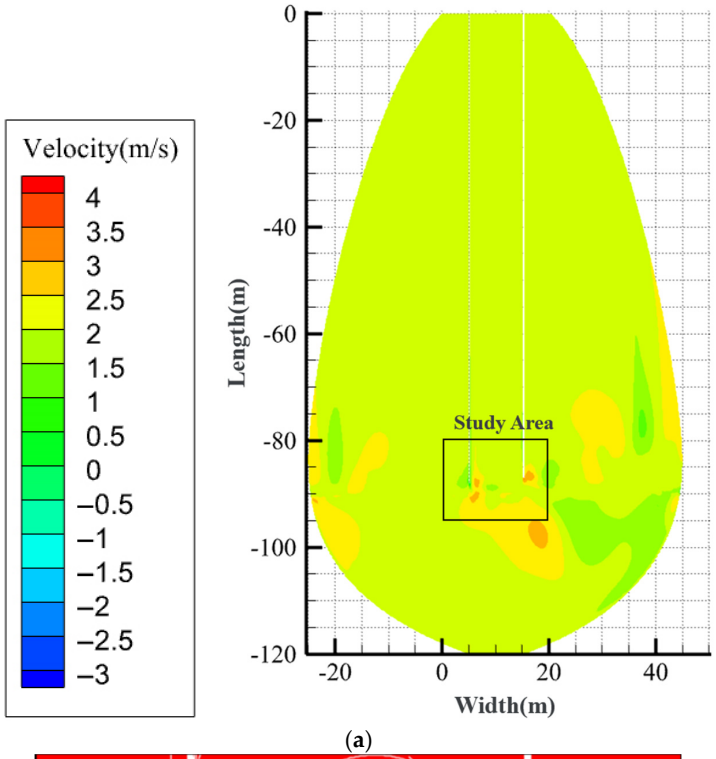

(**a**)

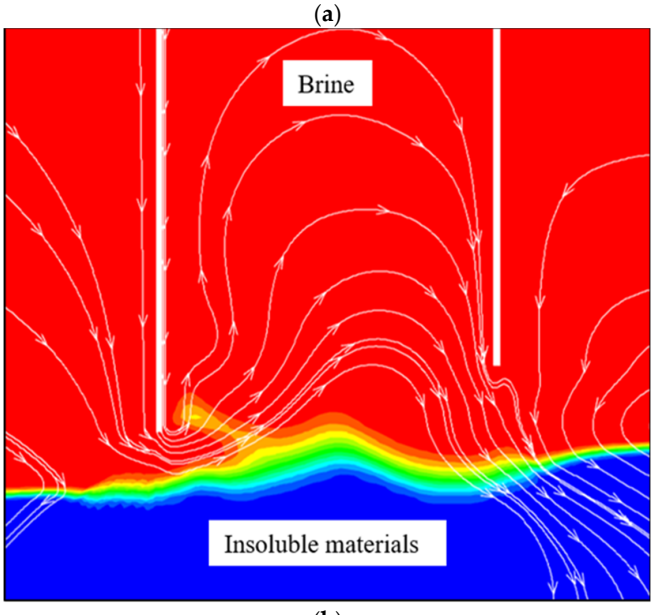

(**b**)

Figure 6. Numerical simulation results. (**a**) overall simulation results; (**b**) streamlines of the injection tubing and discharge tubing regions.

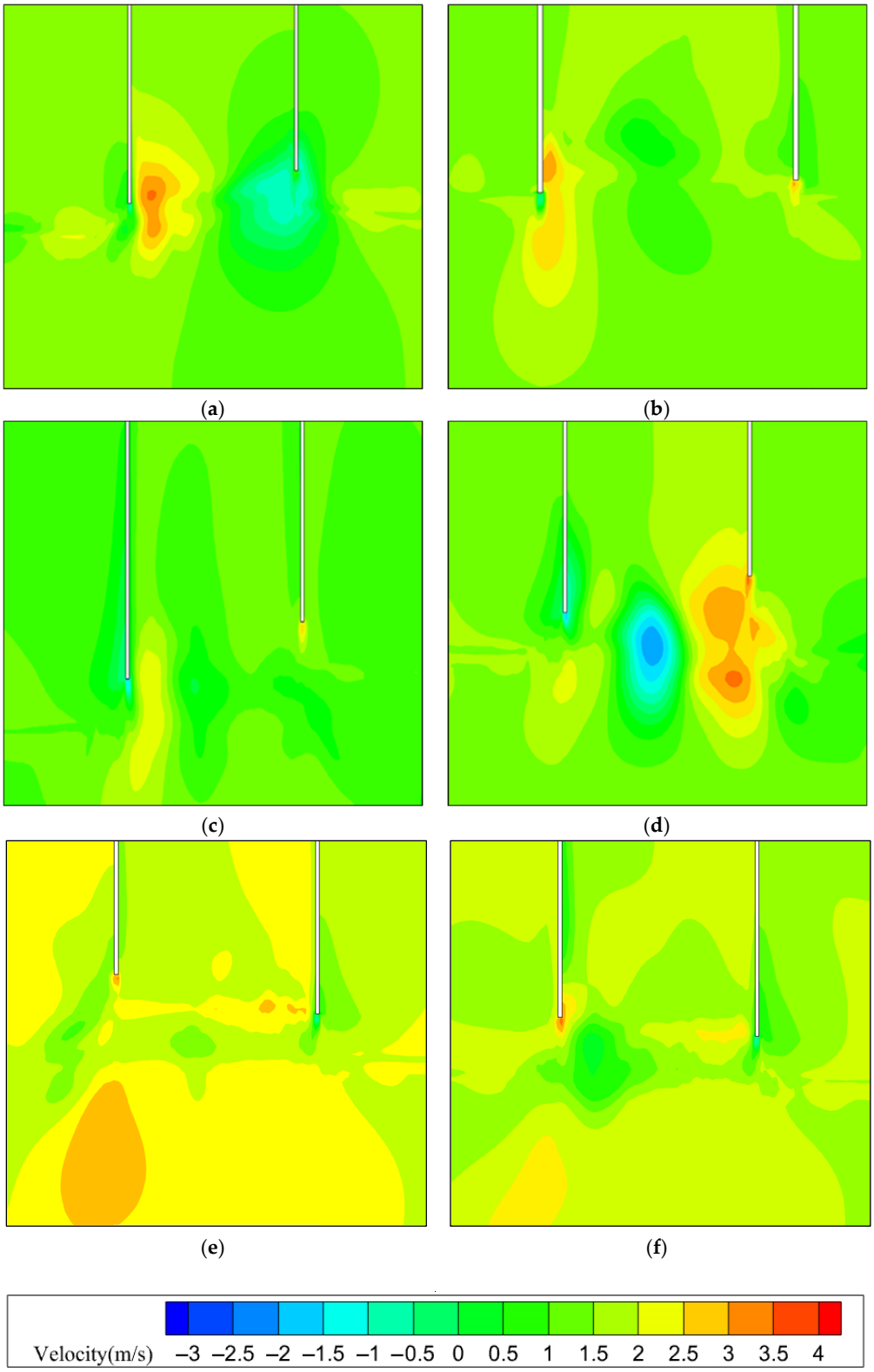

Figure 7. Contour plots of velocity distribution near the injection and discharge tubing: (**a**) H_{IS} = 1 m, H_{DS} = 2 m, D = 139 mm, Q = 90 m^3/h; (**b**) H_{IS} = 2 m, H_{DS} = 1.5 m, D = 168 mm, Q = 160 m^3/h; (**c**) H_{IS} = 0.5 m, H_{DS} = 1 m, D = 168 mm, Q = 90 m^3/h; (**d**) H_{IS} = 2 m, H_{DS} = 1 m, D = 127 mm, Q = 140 m^3/h; (**e**) H_{IS} = 2.5 m, H_{DS} = 1.5 m, D = 114 mm, Q = 120 m^3/h; (**f**) H_{IS} = 1.5 m, H_{DS} = 1 m, D = 139 mm, Q = 140 m^3/h.

3.2. Effect of Flow Rate and Tubing Diameter on Brine and Sediment Behavior

In the SSDW cavern construction process, especially under the combined influence of the injection and discharge flow fields, the interaction between the forces on the particles and the flow field becomes more complex. Due to the proximity of the area directly beneath the injection tubing, where the flow velocity is the highest, insoluble sediment in this region is most easily impacted by the water flow, causing it to float and be drawn into the discharge tubing. Therefore, this study focuses on monitoring the flow velocity of the brine at the sediment surface directly beneath the injection tubing and discharge tubing in numerical simulations to assess the impact of water flow on particle migration. In actual engineering, there is the process of dissolving salt in the cavern (e.g., salt dissolving into the brine), but the dissolution period is very long, and the volume of the cavern changes only slightly. This may cause a temporary imbalance in the flow rates of the injection and discharge tubing, but under constant injection and discharge flow conditions, such volume and flow changes can be ignored. To better align with actual working conditions, considering the potential use of different tubing sizes during the dissolution process, this study utilized four commonly used tubing specifications for numerical simulations: Φ 114.30 mm × 6.88 mm (outer diameter and wall thickness), Φ 127 mm × 7.52 mm, Φ 139 mm × 6.98 mm, and Φ 168.28 mm × 7.32 mm. Corresponding flow rates were configured at 90 m^3/h, 120 m^3/h, 140 m^3/h, and 160 m^3/h, respectively, to comprehensively evaluate the performance and adaptability of these tubing sizes under varying operational conditions. By systematically adjusting the flow rates in conjunction with the tubing dimensions, the simulations aimed to reveal the impact of these parameters on the flow field distribution, and potential risks associated with sediment transport near the tubing inlets. The flow field characteristics associated with these tubing specifications were systematically calculated to investigate the relationship between brine flow velocity and the distance from both the injection tubing and the discharge tubing. This analysis aimed to provide a detailed understanding of how the flow velocity varies spatially within the cavern, particularly in the vicinity of the tubing openings, where the interplay between the injected flow and discharged flow has a significant impact on the transport and deposition of insoluble particles. By examining these velocity distributions, insights were gained into optimizing tubing placement to minimize sediment disturbance and improve the overall efficiency of the cavern development process. Figure 8 illustrates a very obvious relationship between brine flow velocity and the distance from discharge tubing for various tubing sizes. The curve highlights how changes in tubing dimensions influence the flow velocity distribution within the cavern. Specifically, larger tubing diameters tend to reduce flow velocity near the discharge tubing due to the decreased velocity gradient, while smaller tubing diameters result in higher flow velocities at comparable distances. This relationship is critical for understanding how tubing size affects sediment transport and the risk of insoluble particles being drawn into the discharge tubing. By analyzing these curves, optimal tubing dimensions and placements can be identified to enhance the efficiency of brine extraction while minimizing sediment-related blockages. In regions close to the tubing (especially directly beneath), the flow velocity increases significantly, and the curve becomes steeper, indicating that the area near the tubing is most affected by the water flow. As the distance from the tubing increases, the flow velocity follows an exponential or linear decay trend. The influence of tubing size is as follows: small-diameter tubing (e.g., Φ 114.30 mm) exhibits a higher peak flow velocity, and the high-flow region is more concentrated. Since the high flow velocity is concentrated near the discharge tubing, the risk of particles migrating to and being drawn into the discharge tubing increases significantly. On the other hand, large-diameter tubing (e.g., Φ 168.28 mm) shows a wider flow field distribution with an extended high-flow region, but the peak flow velocity decreases, which helps reduce the probability of particle entrainment. Therefore,

larger diameter tubing (e.g., Φ 139 mm or Φ 168.28 mm) is preferred, as this characteristic helps reduce the peak flow velocity near the discharge tubing, lowering the risk of sediment particles being drawn into the discharge tubing and thus improving the safety and stability of the discharge process.

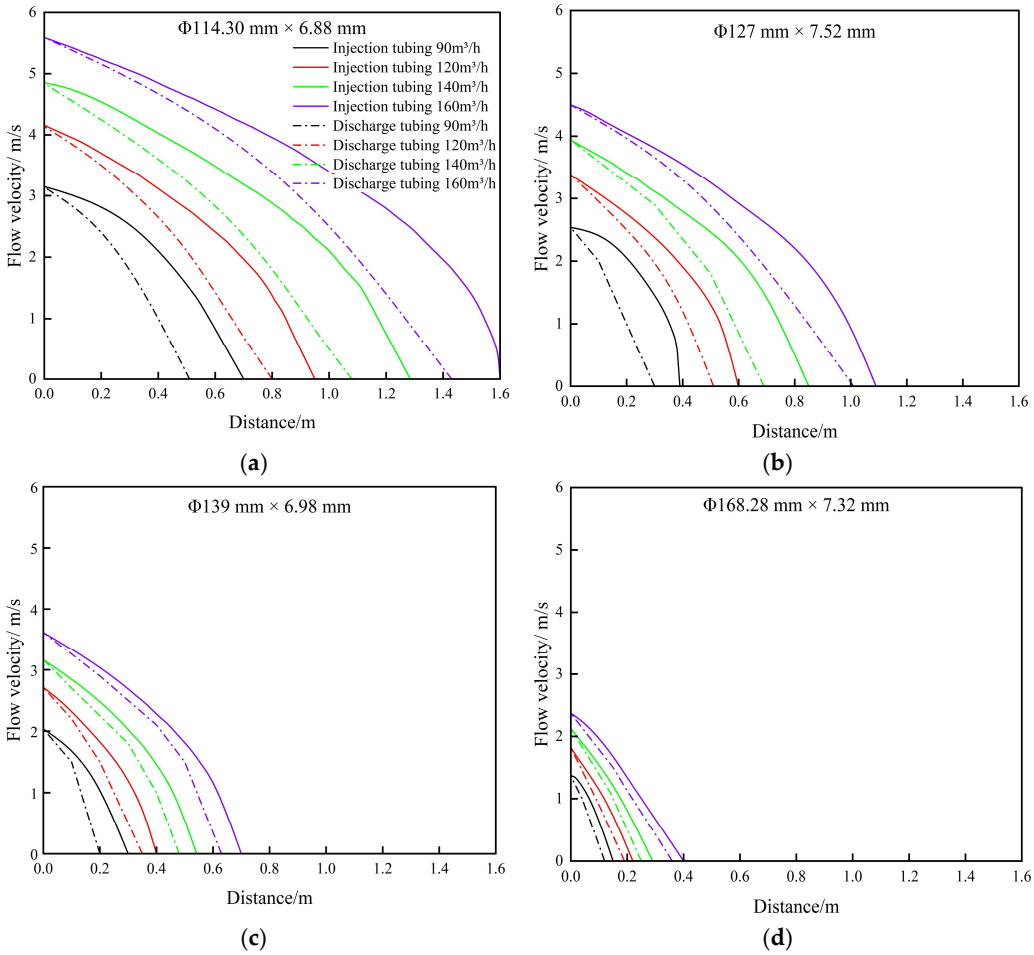

Figure 8. Relationship between flow velocity and distance in the region near the injection tubing and discharge tubing for different tubing sizes: (**a**) both tubing sizes are Φ 114.30 mm × 6.88 mm; (**b**) both tubing sizes are Φ 127 mm × 7.52 mm; (**c**) both tubing sizes are Φ 139 mm × 6.98 mm; (**d**) both tubing sizes are Φ 168.28 mm × 7.32 mm.

As depicted in Figure 8, the brine flow velocity over the sediment surface gradually decreases to 0 m/s as the distance between the tubing ends and the sediment surface increases, following a nonlinear decreasing trend. This phenomenon indicates that the further the distance from the tubing ends, the weaker the influence of the flow field disturbances on the sediment particles. Consequently, the scouring force exerted by the brine on the sediment particles diminishes progressively. Furthermore, an increase in the inner diameter of the discharge tubing results in a noticeable reduction in the overall brine flow velocity. This relationship highlights the dual impact of tubing size on the sediment transport dynamics. Specifically, a larger discharge tubing diameter reduces flow velocity near the tubing, which can lower the likelihood of particle entrainment while also limiting the scouring effect on the sediment surface. This suggests that, under constant flow rates, using larger diameter discharge tubing can effectively reduce the disturbance intensity of the brine on insoluble sediment particles near the discharge tubing, thus reducing the risk of particles being drawn into the tubing. Additionally, the flow velocities below the injection and discharge tubes differ. The injection tubing injects fresh or unsaturated brine

into the cavern, creating high-speed jet flows near the tubing, with concentrated kinetic energy, forming a downward jet with the highest velocity at the injection port, which gradually spreads and decays as the distance from the injection tubing increases. The discharge tubing is responsible for expelling high-concentration brine from the cavern's bottom. Due to the influence of the cavern shape and sediment distribution, the flow field below the discharge tubing is generally more stable, exhibiting attractive flow with gentler dynamics but lower velocities, which gradually diminish to 0 m/s. This occurs because brine is drawn from the sediment surface into the discharge tubing, where the flow velocity decays. In this study, the distance from the tubing-to-sediment surface that does not inhale sediment particles is defined as the critical safety distance. The critical safety distance is defined as the minimum distance between the discharge tubing and the sediment surface where the flow velocity at the sediment surface approaches 0 m/s, ensuring that particles remain undisturbed and are not entrained into the discharge tubing. The critical safety distance is determined based on the flow velocity near the sediment surface. When the flow velocity directly above the sediment decreases to 0 m/s, the fluid has no scouring effect on the sediment particles, thereby preventing particle entrainment into the flow field and subsequent entry into the discharge tubing. This criterion ensures the following: effective brine discharge, saturated brine is removed efficiently without disturbing the sediment bed; minimized sediment ingress, the risk of tubing blockages due to entrained particles is greatly reduced. At this critical distance, saturated brine can be efficiently discharged from the cavity bottom without entraining sediment particles into the discharge tubing. This safe distance acts as a threshold to prevent the upward migration of sediment, thereby mitigating the risk of particle ingress. By carefully optimizing the spacing between the tubing ends and the sediment surface, this can effectively reduce the likelihood of sediment particles entering the discharge tubing. This not only minimizes the risk of blockages but also enhances operational stability and lowers maintenance costs. Furthermore, maintaining an appropriate safe distance improves overall process efficiency by ensuring that sediment transport remains controlled while maximizing the removal of saturated brine from the cavity bottom.

3.3. Effect of Particle Size of Insoluble Sediment

To further assess the impact of insoluble sediment particle diameter on their movement behavior, we conducted simulations for different particle diameters (0.5 mm, 1 mm, 3 mm, and 5 mm), analyzing the changes in the flow field and their effects on sediment movement under different particle diameters and cavern flow rate conditions in order to determine the optimal safety distance between the discharge tubing and the sediment surface. In the study, we assumed the particle density to be 2300 kg/m^3, with the injection and discharge tubing sizes being Φ139 mm × 6.98 mm. The flow velocity below the sediment surface was always maintained at 0 m/s. The critical safety distance between the discharge tubing and the sediment surface is shown in Figure 9 under various particle diameters. The x-axis represents the distance between the tubing end and the sediment surface, while the point where the flow velocity decreases to 0 m/s on the y-axis defines the critical safety distance. This safety distance represents the minimum spacing required to ensure that saturated brine can be effectively discharged without entraining sediment particles.

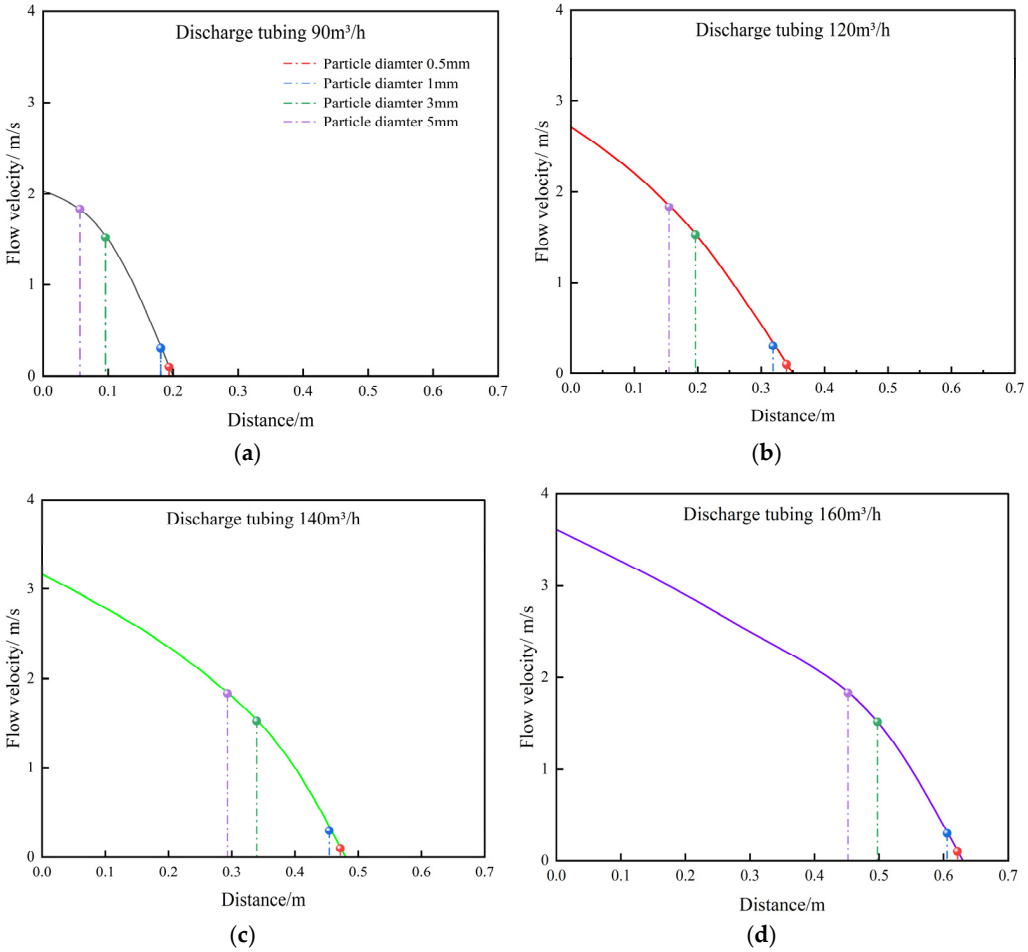

Figure 9. Relationship between flow velocity and corresponding distance for different particle sizes suctioned into the discharge tubing: (**a**) discharge tubing flow rate of 90 m^3/h; (**b**) discharge tubing flow rate of 120 m^3/h; (**c**) discharge tubing flow rate of 140 m^3/h; (**d**) discharge tubing flow rate of 160 m^3/h.

In this study, through numerical simulation and combined with the conclusion of single-well [4,11], the critical starting velocity of particles under different particles was obtained, as shown in Figure 9. In the simulation, the downward extension distance and displacement of the discharge tubing were changed. When the mass of insoluble sediment in the cavity no longer changed significantly and the sediment surface was stable, the tassel corresponding to the sediment surface was the critical starting velocity of the particles, and the distance from the tubing to the sediment surface was the safety critical distance. The findings show that the ideal safety distance from the discharge tubing to the sediment surface progressively increases with increasing flow rate. This is because a higher flow rate enhances the overall flow field strength within the cavern, causing the high-speed region near the tubing to expand, thus requiring a larger distance to avoid particles being drawn into the discharge tubing. The crucial safety distance among the tubing with the sediment surface rapidly shrinks as the particle diameter increases. The numerical simulation results indicate that the velocity required for particles to be entrained into the tubing increases significantly with particle size. Specifically, 0.5 mm particles are entrained at a velocity of 0.1 m/s, 1 mm particles at 0.3 m/s, 3 mm particles at 1.52 m/s, and 5 mm particles at 1.83 m/s. This trend can be attributed to the larger particles requiring higher flow velocities to be entrained due to their greater mass and inertia. As a result, the risk of sediment particles being drawn into the tubing diminishes with increasing particle size, allowing the tubing to be positioned closer to the sediment surface without compromising safety.

This is because larger particles have a greater mass and are more significantly affected by gravity, requiring higher brine velocities to be transported, while the brine velocity near the tubing decays rapidly with increasing distance. Therefore, larger particles are less likely to be drawn in near the tubing. Conversely, smaller particles are more easily disturbed by the flow field, thus requiring a larger safety distance to reduce the risk of entrainment. For example, the optimum safety distances for particle diameters of 0.5 mm, 1 mm, 3 mm, and 5 mm at a flow rate of 160 m^3/h are 0.62 m, 0.60 m, 0.50 m, and 0.40 m. This shows that for smaller particles (e.g., 0.5 mm and 1 mm), the distance variation is small, but for larger particles (e.g., 3 mm and 5 mm), there is a significant difference. When the particle diameter is tiny (e.g., $\leq$3 mm), the reduction in safety distance is limited, and it can easily lead to the accumulation of insoluble sediment particles near the discharge tubing, increasing the risk of salt crystal formation and particle blockage. This risk is especially prominent under high flow rate conditions. Therefore, in actual engineering, to guarantee the discharge tubing's safe operation, the primary criterion for determining the positioning of the two tubing ends should be to prevent particles from being drawn into the discharge tubing.

3.4. Effect of Insoluble Sediment Density

The insoluble particle types in salt rock deposits are diverse, and their density distribution exhibits significant differences. When designing a dual-well cavern, the discharge tubing's downward extension distance is crucial for determining how the flow field is distributed at the cavern bottom and how the insoluble particles move. Therefore, dynamically adjusting the downward extension distance of the discharge tubing based on sediment density during the dissolution process is of particular importance. If the discharge tubing is too close to the sediment surface, high flow velocities may cause insoluble particles to be drawn into the tubing, increasing the risk of blockages. However, the saturated brine at the cavern bottom might not be adequately discharged if the particle density and diameter are high and the discharge tubing is too far from the sediment surface. This would impact the overall homogeneity of the dissolution process and the gas storage cavern's utilization efficiency.

When the discharge tubing size is Φ 139 mm $\times$ 6.98 mm, Figure 10, which is based on numerical simulations, illustrates the relationship between the initial velocity for particles to be drawn into the discharge tubing and the particle diameter under various particle density situations. The simulation results reveal a clear trend: as the particle diameter and density increase, the starting velocity required to entrain the particles into the discharge tubing also rises significantly. The main cause of this behavior is that larger and denser particles are subject to stronger gravitational and inertial forces, which necessitate higher flow velocities in order to overcome their resistance to motion. Additionally, the simulation demonstrates that when the separation between the sediment surface and the discharge tube grows, the flow field intensity gradually weakens, the local flow velocity decreases, and the disturbance and migration of insoluble particles also decrease. As the particle diameter increases, the gravitational and inertial forces acting on the particles increase significantly, and a higher flow velocity is required to draw them into the tubing. Therefore, the distance between the discharge tubing and the sediment surface can be appropriately reduced to ensure the smooth discharge of saturated brine from the cavern bottom. However, for smaller particles, due to their lighter mass, the fluid can overcome their gravitational and adhesive forces at lower speeds, and thus the discharge tubing needs to be raised appropriately to reduce the likelihood of particles entering the tubing. Furthermore, the particle density significantly affects the ease with which the particles are entrained by the fluid. At the same flow velocity, particles with a higher density, due to their greater mass per unit volume, are more difficult to entrain than those with a lower density. For example,

particles having a 2500 kg/m^3 density require a significantly higher starting velocity to be drawn into the tubing compared to particles with a density of 2300 kg/m^3, even if their diameters are the same. This indicates that in practical operations, the particle diameter and density should be used to optimize the discharge tubing's downward extension distance, ensuring the effective discharge of saturated brine while minimizing the possibility of insoluble particles getting into the tubing. This approach can improve the efficiency and safety of the dissolution process.

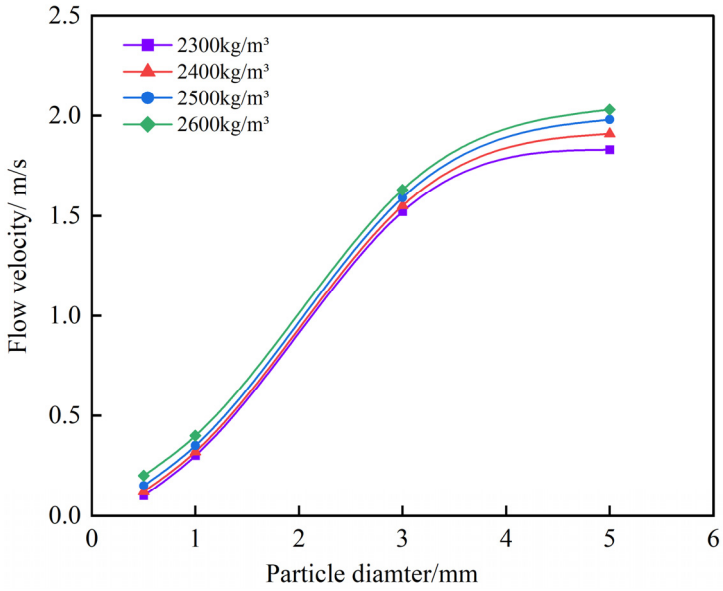

Figure 10. Relationship between flow velocity and particle size for insoluble sediments with different densities being suctioned into the discharge tubing.

3.5. Optimization of Tubing-to-Sediment Distance

In the optimization of tubing-to-sediment surface distance during brine extraction in SSDW salt caverns, multiple factors influence the behavior and transport of insoluble sediment particles. This section summarizes the effects of particle size, density, brine flow velocity, tubing diameter, and tubing-to-sediment distance on sediment transport dynamics, using the critical safety distance as a key optimization parameter. The optimization process uses numerical simulations to identify the critical safety distance under varying flow conditions and particle characteristics. The factors influencing this distance are summarized below.

Larger tubing diameters (e.g., Φ 168.28 mm × 7.32 mm) result in lower fluid velocities at the tubing outlet for a given flow rate due to the increased cross-sectional area. This reduces the velocity gradient near the sediment surface and decreases the risk of particle entrainment, allowing for a smaller critical safety distance. Smaller tubing diameters (e.g., Φ 114.30 mm × 6.88 mm) produce higher outlet velocities, increasing the scouring effect on the sediment surface. This necessitates a larger critical safety distance to avoid disturbing sediment particles. Larger tubing diameters reduce the risk of sediment entrainment and allow for closer tubing positioning, while smaller diameters require more conservative safety distances.

When the discharge tubing is positioned too close to the sediment surface, the high-velocity flow near the injection tubing can disturb and entrain sediment particles, especially smaller or lower-density particles. This increases the risk of blockages and system inefficiencies. Excessive distances reduce the flow velocity at the sediment surface, ensuring particle stability but potentially leaving saturated brine near the sediment surface undisturbed. This affects the uniformity of the dissolution process and reduces the efficiency of brine

extraction. The tubing-to-sediment distance must balance these effects, ensuring effective brine removal without disturbing sediment particles. Numerical simulations in this study identified optimal distances for different particle sizes (e.g., 0.62 m for 0.5 mm particles at 160 m^3/h).

Sediment particles with smaller diameters (e.g., 0.5 mm) are more easily entrained due to their lower mass and inertial resistance. These particles require lower flow velocities to reach their starting velocity, which increases the likelihood of entrainment into the discharge tubing. To mitigate this risk, the critical safety distance must be larger for smaller particles to reduce the flow velocity at the sediment surface. Larger particles (e.g., 3–5 mm) possess greater mass and inertial resistance, requiring significantly higher flow velocities to become entrained. Consequently, the critical safety distance can be reduced for larger particles, as they are less likely to be disturbed by the flow field. However, if the distance is too short, localized high-velocity regions near the tubing can still disturb larger particles, especially under high flow rates.

Higher density particles (e.g., 2500 kg/m^3) require greater flow velocities to overcome their gravitational and inertial forces, making them less susceptible to entrainment. Lower-density particles (e.g., 2300 kg/m^3) are more easily entrained under the same flow conditions, requiring a greater critical safety distance to reduce the flow velocity near the sediment surface. As particle density increases, the critical safety distance decreases due to the reduced risk of entrainment. However, for heterogeneous sediment beds with varying densities, the optimization process must consider the lowest-density particles as the primary constraint.

The critical safety distance is directly influenced by particle size, density, flow velocity, and tubing diameter. Smaller particles and higher flow rates require larger distances, while larger particles and lower flow rates allow for closer positioning. The optimization criterion is based on reducing the sediment surface flow velocity to 0 m/s, ensuring particle stability while maximizing brine extraction efficiency. Larger tubing diameters are recommended for reducing sediment disturbance and minimizing the critical safety distance. By integrating these considerations, the study provides a systematic framework for optimizing the tubing-to-sediment surface distance in SSDW salt caverns, ensuring efficient and safe cavern development.

4. Summary and Conclusions

(1) Mastering the changes in the brine flow field near the injection and discharge tubing and the migration of insoluble sediment particles is crucial for determining the safe downward extension depth of the discharge tubing during SSDW cavern construction. The flow field and sediment transport patterns were examined using a numerical simulation model. The study simulated different cavern construction flow rates and tubing sizes and detailed the critical safe distance for the downward extension of tubing under different working conditions through data graphs; the study also explored how the size of the tubing column affects this distance. The findings provide technical support for optimizing the dual-well cavern construction process.

(2) The safe downward extension distance is influenced by multiple factors, including particle diameter, particle density, flow rate, tubing size, and the tubing-to-sediment surface distance. The study shows that larger particles and higher particle densities require higher flow velocities for entrainment, reducing their likelihood of being drawn into the tubing. Conversely, smaller particles and lower flow rates necessitate greater safety distances to avoid sediment intrusion. For example, under a flow rate of 160 m^3/h, the safety distance decreases as tubing diameter increases, as larger diameters result in lower outlet velocities and less sediment disturbance. These

findings highlight the need to balance all parameters to achieve the recommended design criterion of "no suction of insoluble particles", ensuring efficient brine discharge and sediment stability.

(3) A systematic optimization approach was applied to determine the ideal tubing-to-sediment surface distance based on real project parameters. The numerical simulations revealed that optimizing flow rates, tubing dimensions, and placement can significantly enhance cavern dissolution efficiency, improve cavern shape uniformity, and minimize sediment-related risks. However, the study also points to potential challenges in accounting for geological heterogeneities, such as fractures or irregular salt cavern shape, which may alter flow behavior. Future research should focus on integrating these complexities into the model and exploring their impact on long-term cavern stability and storage capacity, further refining design guidelines for similar projects.

Author Contributions: Conceptualization, L.W.; Methodology, Z.C.; Software, J.H. (Jiang He); Validation, Y.Z.; Formal analysis, J.H. (Junming Huang); Data curation, H.Y. All authors have read and agreed to the published version of the manuscript.

Funding: This research was funded by the National Natural Science Foundation of China (Grant No. 52192624).

Data Availability Statement: The original contributions presented in this study are included in the article. Further inquiries can be directed to the corresponding author.

Conflicts of Interest: Lei Wang, Zheng Chu, Jiang He, Yujia Zhai and Junming Huang are employed by the Sinopec Research Institute of Petroleum Engineering Co., Ltd. The authors declare that the research was conducted in the absence of any commercial or financial relationships that could be construed as a potential conflict of interest.

References

1. Li, Q.; Li, Q.; Wu, J.; Li, X.; Li, H.; Cheng, Y. Wellhead Stability During Development Process of Hydrate Reservoir in the Northern South China Sea: Evolution and Mechanism. *Processes* **2024**, *13*, 40. [CrossRef]
2. Li, Q.; Li, Q.; Cao, H.; Wu, J.; Wang, F.; Wang, Y. The Crack Propagation Behaviour of CO_2 Fracturing Fluid in Unconventional Low Permeability Reservoirs: Factor Analysis and Mechanism Revelation. *Processes* **2025**, *13*, 159. [CrossRef]
3. Botho, S. New development in solution mining technology. In Proceedings of the SMRI Spring 1997 Meeting, Cracow, Poland, 11–14 May 1997.
4. Li, P.; Li, Y.; Shi, X.; Zhao, K.; Liu, X.; Ma, H.; Yang, C. Prediction Method for Calculating the Porosity of Insoluble Sediments for Salt Cavern Gas Storage Applications. *Energy* **2021**, *221*, 119815. [CrossRef]
5. Liu, W.; Zhang, Z.; Chen, J.; Jiang, D.; Wu, F.; Fan, J.; Li, Y. Feasibility Evaluation of Large-Scale Underground Hydrogen Storage in Bedded Salt Rocks of China: A Case Study in Jiangsu Province. *Energy* **2020**, *198*, 117348. [CrossRef]
6. Chen, J.; Lu, D.; Liu, W.; Fan, J.; Jiang, D.; Yi, L.; Kang, Y. Stability Study and Optimization Design of Small-Spacing Two-Well (SSTW) Salt Caverns for Natural Gas Storages. *J. Energy Storage* **2020**, *27*, 101131. [CrossRef]
7. Li, J.; Shi, X.; Wang, T.; Yang, C.; Li, Y.; Ma, H.; Ma, X.; Shi, H. A Prediction Model of the Accumulation Shape of Insoluble Sediments during the Leaching of Salt Cavern for Gas Storage. *J. Nat. Gas Sci. Eng.* **2016**, *33*, 792–802. [CrossRef]
8. Li, P.; Li, Y.; Shi, X.; Zhao, K.; Liang, X.; Ma, H.; Yang, C.; Liu, K. Compaction and Restraining Effects of Insoluble Sediments in Underground Energy Storage Salt Caverns. *Energy* **2022**, *249*, 123752. [CrossRef]
9. Sun, X.; Tao, L.; Zhao, Y.; Qu, J.; Yao, D.; Li, Z. Numerical Simulation of Hole Cleaning of a Horizontal Wellbore Model with Breakout Enlargement Section. *Mathematics* **2023**, *11*, 3070. [CrossRef]
10. Li, H.; Deng, J.; Wanyan, Q.; Feng, Y.; Kamgue Lenwoue, A.R.; Luo, C.; Hui, C. Numerical Investigation on Shape Optimization of Small-Spacing Twin-Well for Salt Cavern Gas Storage in Ultra-Deep Formation. *Energies* **2021**, *14*, 2859. [CrossRef]
11. Wang, T.; Chai, G.; Cen, X.; Yang, J.; Daemen, J.J.K. Safe Distance between Debrining Tubing Inlet and Sediment in a Gas Storage Salt Cavern. *J. Pet. Sci. Eng.* **2021**, *196*, 107707. [CrossRef]
12. Kazemi, H.; Jessen, F.W. Mechanism of Flow and Controlled Dissolution of Salt in Solution Mining. *Soc. Pet. Eng. J.* **1964**, *4*, 317–328. [CrossRef]
13. He, Q.; Feng, Y.; Yuan, G.; Ban, F.; Guan, Y.; Xu, N. Experimental Study of Dual-Well Gas Injection and Brine Discharge in Salt Cavern Sediment Space. *Gas Sci. Eng.* **2023**, *117*, 205084. [CrossRef]

14. Ding, J.; Gidaspow, D. A Bubbling Fluidization Model Using Kinetic Theory of Granular Flow. *AIChE J.* **1990**, *36*, 523–538. [CrossRef]
15. Mokhtari, M.; Tutuncu, A.N.; Weldu Teklu, T.W. A Numerical Modeling Study for the Impact of Casing Drilling on Wellbore Stability. In Proceedings of the SPE Unconventional Resources Conference, Calgary, AB, Canada, 5 November 2013; SPE: Calgary, AB, Canada, 2013; p. SPE-167166-MS.
16. Ghazanfari, V.; Imani, M.; Shadman, M.M.; Amini, Y.; Zahakifar, F. Numerical Study on the Thermal Performance of the Shell and Tube Heat Exchanger Using Twisted Tubes and Al_2O_3 Nanoparticles. *Prog. Nucl. Energy* **2023**, *155*, 104526. [CrossRef]
17. Walton, O.R.; Braun, R.L. Viscosity, Granular-temperature, and Stress Calculations for Shearing Assemblies of Inelastic, Frictional Disks. *J. Rheol.* **1986**, *30*, 949–980. [CrossRef]
18. Brilliantov, N.V.; Pöschel, T. Rolling Friction of a Viscous Sphere on a Hard Plane. *Europhys. Lett.* **1998**, *42*, 511–516. [CrossRef]
19. Mathiesen, V.; Solberg, T.; Hjertager, B.H. Predictions of Gas/Particle Flow with an Eulerian Model Including a Realistic Particle Size Distribution. *Powder Technol.* **2000**, *112*, 34–45. [CrossRef]
20. Lun, C.K.K.; Savage, S.B.; Jeffrey, D.J.; Chepurniy, N. Kinetic Theories for Granular Flow: Inelastic Particles in Couette Flow and Slightly Inelastic Particles in a General Flowfield. *J. Fluid Mech.* **1984**, *140*, 223–256. [CrossRef]
21. Huilin, L.; Gidaspow, D.; Bouillard, J.; Wentie, L. Hydrodynamic Simulation of Gas–Solid Flow in a Riser Using Kinetic Theory of Granular Flow. *Chem. Eng. J.* **2003**, *95*, 1–13. [CrossRef]
22. Schiller, A.N.L. Uber Die Grundlegenden Berechnungen Beider Schwerkraftaufbereitung. *Z. Ver. Dtsch. Ing.* **1933**, *77*, 318–320.
23. Cioncolini, A.; Cassineri, S.; Duff, J.; Curioni, M.; Scenini, F. Micro-Orifice Single-Phase Flow at Very High Reynolds Number. *Exp. Therm. Fluid Sci.* **2018**, *91*, 35–40. [CrossRef]
24. Jiang, D.; Li, Z.; Liu, W.; Ban, F.; Chen, J.; Wang, Y.; Fan, J. Construction Simulating and Controlling of the Two-Well-Vertical (TWV) Salt Caverns with Gas Blanket. *J. Nat. Gas Sci. Eng.* **2021**, *96*, 104291. [CrossRef]
25. Li, Y.; Peng, G.; Tang, J.; Zhang, J.; Zhao, W.; Liu, B.; Pan, Y. Thermo-Hydro-Mechanical Coupling Simulation for Fracture Propagation in CO_2 Fracturing Based on Phase-Field Model. *Energy* **2023**, *284*, 128629. [CrossRef]
26. Li, Y.; Peng, G.; Du, T.; Jiang, L.; Kong, X.-Z. Advancing Fractured Geothermal System Modeling with Artificial Neural Network and Bidirectional Gated Recurrent Unit. *Appl. Energy* **2024**, *372*, 123826. [CrossRef]

Disclaimer/Publisher's Note: The statements, opinions and data contained in all publications are solely those of the individual author(s) and contributor(s) and not of MDPI and/or the editor(s). MDPI and/or the editor(s) disclaim responsibility for any injury to people or property resulting from any ideas, methods, instructions or products referred to in the content.